Radar Area Chart as a Framework for Quantitative Analysis of Electronic Noses in Monitoring Water Stress in Plants

Paulo S. de P. Herrmann[1], Matheus Santos Luccas[2]
[1]Embrapa Instrumentation (CNPDIA), São Carlos, SP, Brazil
[2] Institute of Mathematics and Computer Sciences, University of São Paulo, São Carlos, SP, Brazil
e-mail: paulo.herrmann@embrapa.br, matsluccas@gmail.com

***Abstract*—Water stress is a major factor limiting the productivity of soybean (Glycine max L.) worldwide. Early detection is crucial for implementing timely irrigation strategies. Electronic noses (E-noses) offer a promising, non-invasive approach for monitoring plant gas emissions. This work extends our previous publication and proposes the quantitative use of radar chart areas as a novel metric to evaluate and compare the sensitivity of individual E-nose sensors in detecting water stress. By calculating the polygon area formed by the normalized response peaks of a six-sensor array, we transform multivariate sensor data into a single, comparable index. This approach was applied to data from soybean plants subjected to controlled irrigation and water stress conditions over 21 days. The results demonstrate that the radar chart area metric effectively captures the temporal progression of stress, showing a distinct divergence between irrigated and non-irrigated plants after the onset of water stress. The proposed area-based metric provides a comprehensive, quantitative tool for sensor performance evaluation, enhancing the interpretation of E-nose data. This methodological advancement not only validates the radar chart area as a robust indicator of plant stress but also paves the way for more precise, data-driven decisions in precision agriculture applications.**

***Keywords*—Radar charts; Electronic nose; Precision agriculture; Water stress; Volatile Organic Compounds.**

I. Introduction

This work extends our previous publication [1] and builds upon recent advances that have introduced electronic noses (E-noses) as innovative tools for monitoring plant health. E-noses consist of sensor arrays capable of detecting specific patterns of Volatile Organic Compounds (VOCs) emitted by plants under stress conditions (see Figure 1). Changes in VOC profiles, which can serve as early indicators of water stress even before visual symptoms appear [2], are a key focus of this extension.

Soybean (*Glycine max* L.) is a vital crop, serving as a key source of protein and oil for human consumption and animal feed. Water stress remains one of the most critical abiotic stresses affecting soybean growth and yield, leading to global economic losses. Traditional methods for detecting water stress involve physiological measurements and visual assessments, which can be labor-intensive and subjective.

E-nose technology has been extensively evaluated in experiments employing statistical techniques such as Principal Component Analysis (PCA) and Linear Discriminant Analysis (LDA) to reduce the dimensionality of the collected data [4]. Among these, the dynamic mode has been a distinguished method for identifying the most informative features that distinguish between varying stress levels. In this context, the peak response values of semiconductor sensors during VOC adsorption and desorption have been utilized as effective features for such analysis [2], with radar charts serving as a visualization tool for this purpose.

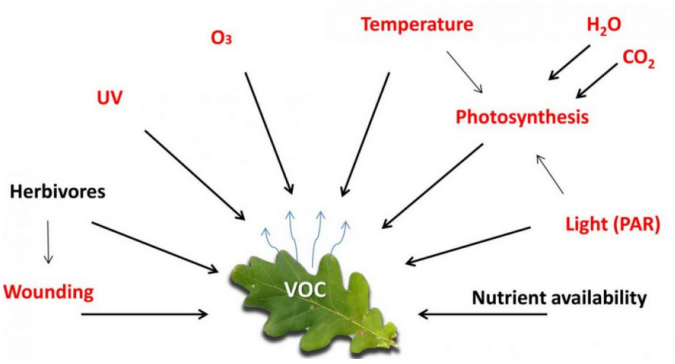

Fig. 1. VOCs and factors affecting plant emissions [3].

A typical E-nose system, as illustrated in Figure 2, consists of several key components including sensor arrays, signal transducers, and data processing units.

Also known as a spider plot, star plot, or Kiviat figure [5], the radar chart is more than just a graphical technique; it serves as a crucial methodological component in this study. It provides a straightforward way to display multivariate data on a two-dimensional plane, facilitating the visualization and comparison of sensor responses. This visualization ultimately enables the evaluation of sensor sensitivity [2].

A radar chart presents multivariate data on axes that radiate outward from a central point. As illustrated in Figure 3, each axis represents a distinct variable, with data points plotted along these axes. Connecting these points forms a polygon, and calculating the area of this polygon can yield valuable quantitative insights into the dataset [6].

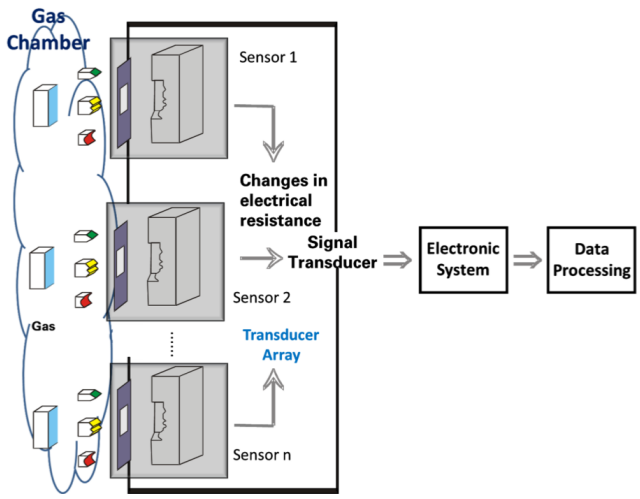

Fig. 2. Block diagram of an E-nose and its components, including sensors, signal transducer, electronic system, and data processing.

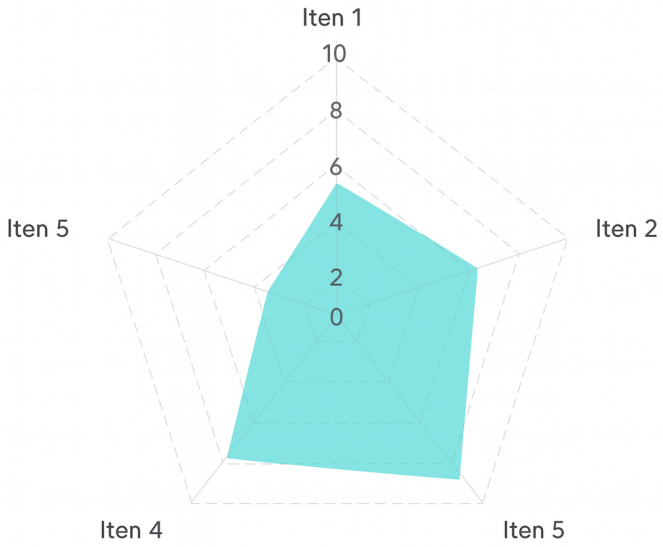

Fig. 3. Radar Chart with an Area.

A. Economic and Agricultural Context

Soybean cultivation occupies a strategic position in Brazilian agriculture [7]. This economic importance amplifies the impact of water stress, which can cause yield losses of up to 40% in soybean crops [8]. The development of affordable, non-invasive monitoring tools is therefore critical for sustainable agricultural management and food security.

Recent interdisciplinary collaborations combining engineering, physics, geosciences, plant sciences, ecophysiology, computer science, and instrumentation have advanced non-invasive phenotyping techniques [9]. Among these, E-nose technology offers particular promise due to its ability to detect VOCs emitted by plants under stress conditions in a non-invasive setup [10] [11].

B. VOC emissions throughout the day

Plant responses to water stress involve complex physiological and biochemical adaptations, including stomatal closure, growth repression, and activation of respiration pathways [12]. Recent studies have identified specific biomarkers, such as isoprene and hexanal, which serve as early, non-visible indicators that soybean plants are metabolically fighting to retain water before visible wilting occurs [13]. The relevance of compounds like hexanal is underscored by post-harvest studies, where it has been identified as a key marker of lipid peroxidation and oxidative deterioration in soybean grains, directly linked to stress-induced damage [14]. These VOC changes can precede visual symptoms by several days, providing a critical window for intervention.

Transpiration dynamics play a crucial role in these emissions, with Vapor Pressure Deficit (VPD) influencing stomatal behavior throughout the day [15]. Studies have shown distinct patterns between low VPD periods (7–11 AM) and high VPD periods (11 AM–3 PM), justifying our measurement protocol at 9:30 AM and 3:30 PM to capture these diurnal variations.

The ability to detect these subtle metabolic shifts through non-invasive methods like E-nose technology represents a significant advancement over traditional visual assessments. Our radar chart area methodology aims to capture these early VOC pattern changes, enabling proactive rather than reactive agricultural management.

”

1) Objectives and structure: Takenaka et al. [16] provided a method for evaluating the accessibility of a facility location using the area of a radar chart. The authors argue that the area of a radar chart is a more stable measure of accessibility than other metrics.

The main objectives of this investigation are:

1) To develop a method utilizing radar chart areas to evaluate the sensitivity of E-nose sensors in detecting water stress in soybean plants;
2) To identify which sensors within the E-nose array are most responsive to VOC changes associated with water stress;
3) To assess the effectiveness of radar chart areas as a quantitative metric for sensor performance in agricultural monitoring applications.

The remainder of this paper is structured as follows. Section III presents the materials and methods. Section IV discusses the experimental results. Finally, Section V concludes the article and outlines directions for future work.

II. State of the Art

This section presents a survey of relevant publications and investigations that situate our work within the current research landscape.

A. Bibliographic References for Radar Chart Area Calculation as Quantitative Result: a Survey

This section provides bibliographic references demonstrating that the calculation of graphical area in multidimensional radar charts serves as a quantitative result for performance measurement, evaluation, and comparison. The references are organized by methodology and application domain, with emphasis on papers that explicitly use area calculations as quantitative metrics.

1) Radar Chart Area Calculations Use:

a) Wind Power Accommodation Evaluation [17]: The authors proposed an improved radar chart method that replaced traditional fan-shaped sectors with quadrilateral evaluation regions. They constructed new area and perimeter vectors for the radar chart to provide comprehensive evaluation metrics. The area vector represented the aggregation degree of wind power accommodation ability, while the perimeter vector reflected the balance degree across different indicators.

This methodology allows for the evaluation of wind power systems based on both macroscopic indicators (e.g., installed capacity, power generation) and microscopic indicators (e.g., voltage stability, power quality).

b) Estimation Performance Evaluation [18]: The authors designed a comprehensive measure based on the radar chart's fan area and fan arc length, which they formalized into a radar chart index (RCI) that combines multiple performance measures through weighted components. Within this framework, the fan area served as the key quantitative component for calculating the overall estimation performance index. The proposed mathematical framework defines an index that integrates multiple otherwise incomprehensive measures, using fan area and arc length as core quantitative metrics, and is supported by case studies that demonstrate its utility through numerical comparisons. In application, this methodology enables the evaluation of estimation algorithms and statistical estimators across a range of performance criteria.

c) Principal Component Analysis Integration [19]: The authors combined PCA with radar charts to create a comprehensive evaluation model. Their key innovation was using the area of the radar chart polygon as a synthetic quantitative indicator, which they implemented by first applying PCA to transform and weight the original variables. The methodology involved applying PCA to reduce dimensionality, constructing a radar chart from the principal components, and then calculating the polygon area to serve as a comprehensive evaluation score, enabling ranking and comparison based on its magnitude. In application, this model facilitates general comprehensive evaluation and performance assessment across multiple domains.

d) Mathematical Foundations of Synthetic Indicators [20]: The authors established rigorous mathematical foundations for radar-chart-based synthetic indicators. They developed formal notation for radar-map-induced polygons, employed an analogue of the scalar product of vectors, proved theorems on polygon fields induced by radar maps, and constructed concentration indicators from radar-chart polygonal areas. Their key mathematical contributions include formally proving that radar chart polygons can serve as synthetic meters, constructing concentration measures (analogous to the Gini coefficient) from radar areas, and creating a theoretical framework for comparing alternatives using polygon-derived metrics. In application, this methodology is designed for socioeconomic indicator analysis, material deprivation studies, and country-level comparisons.

2) Radar Charts for Quantitative Shape Analysis:

a) Biomechanics and Materials Science [21]: The authors used permuted radar charts to create closed polygonal profiles representing multi-property mechanical performance and applied shape descriptors to these polygons for quantitative comparison. Specifically, they utilized polygon area as a measure of overall performance and shape metrics to compare performance distributions. This method is designed for application in comparative biomechanics, biological materials performance assessment, and functional morphology studies.

b) Construction Industry Performance [22]: The authors applied the radar chart to evaluate the performance of construction companies. Their quantitative method used radar chart areas to measure and compare operational performance across multiple dimensions, and they demonstrated how substituting traditional line or bar charts with area-based radar representations could provide holistic performance metrics.

3) Multi-Criteria Decision Making Applications:

a) Visual Filtering and Decision Support [23]: The authors constructed radial graphic representations with normalization to enable quantitative visual filtering of alternatives. Their system utilized radar-like plots with area-based comparisons to filter alternatives based on threshold criteria, provide quantitative filtering reductions, and support interactive multi-criteria selection. This approach was developed for application in multi-criteria decision support systems and alternative selection.

b) Educational Assessment [24]: The authors employed radar-like visual profiles for multi-competency comparison and quantitative assessment. Their tool used radar chart representations to provide numerical comparisons across student attributes and capabilities, making it applicable for student capability assessment and educational performance measurement.

4) Additional Supporting References:

a) Eco-efficiency Index Development [25]: The authors used radar charts as part of developing composite eco-efficiency indices, treating the visual representation as a quantitative tool for environmental performance comparison. Their methodology was designed for application in environmental performance assessment and sustainability metrics.

5) Mathematical Foundations and Area Calculation Methods:

a) General Polygon Area Formula: For a radar chart with n dimensions, where each dimension has a normalized value v_i (typically scaled 0-1 or 0-100) at angle $\theta_i = 2\pi i/n$, the

polygon area can be calculated as:

$$\text{Area} = \frac{1}{2} \sum_{i=1}^{n} (v_i \times v_{i+1} \times \sin(\theta_{i+1} - \theta_i)) \quad (1)$$

For equally-spaced axes (regular polygon case):

$$\text{Area} = \frac{n}{2} \times \sin\left(\frac{2\pi}{n}\right) \times \sum_{i=1}^{n} (v_i \times v_{i+1}) \quad (2)$$

where $v_{n+1} = v_1$ (closing the polygon).

b) Alternative Formulations: Several papers reference alternative area-based metrics:

- *Fan Area Method* [18]: Calculates area of individual sectors/fans and aggregates them with weights
- *Vector-Based Area* [17]: Constructs area vectors representing aggregation across multiple sub-regions
- *Normalized Area Index*: Area ratio comparing actual performance polygon to maximum possible area (all dimensions at maximum value)

6) Key Findings and Conclusions: The survey demonstrates that radar chart area calculations constitute a robust quantitative metric. This rigor stems from a formal mathematical foundation, including proofs and theorems that establish its theoretical validity. Its practical utility is corroborated by successful applications across diverse fields of study. Furthermore, the area metric provides distinctive comparative power, enabling objective numerical analysis among different alternatives. Ultimately, its principal virtue lies in its aggregation capability, efficiently synthesizing complex, multi-dimensional data into a single, interpretable quantitative indicator.

a) Application Domains: Radar chart area calculations have been validated as robust quantitative metrics through their successful application across diverse research domains. Within Engineering, they are utilized for evaluating wind power systems and estimation algorithms. In Biomechanics, these calculations assess the performance of biological materials. The field of Economics employs them to analyze socioeconomic indicators and derive concentration measures, while Education applies them for student capability assessment. Furthermore, in Business contexts, they facilitate the evaluation of construction company performance and eco-efficiency metrics. Finally, in Decision Science, radar chart areas provide foundational support for multi-criteria decision-making and systematic alternative selection.

b) Methodological Advantages: This survey highlights several distinct advantages of employing radar chart area as a quantitative metric, primarily its capacity for visual-quantitative integration, which merges intuitive graphical representation with objective numerical measurement. It further enables multi-dimensional synthesis by aggregating multiple disparate criteria into a single, comparable index. Crucially, the derived area exhibits sensitivity to balance, reflecting both the magnitude and the relative distribution of values across dimensions. The method demonstrates strong normalization compatibility, functioning effectively with standardized data, and provides comparative clarity by facilitating the straightforward ranking and benchmarking of alternatives. Collectively, this comprehensive bibliographic foundation firmly establishes radar chart area calculation as a quantitatively robust methodological approach, thereby justifying its application in this study to evaluate E-nose sensor sensitivity to water stress in soybean plants.

7) Recommended Core References: For researchers seeking to use radar chart area calculations as quantitative results, the core references summarized in Table I provide the strongest evidence across different domains.

III. Materials and Methods

Below are presented all the materials and methods used in this work, as well as the equations used to obtain the results.

A. Plant Material and Experimental Design

Soybean seeds (*Glycine max* L.) were germinated and grown in controlled greenhouse conditions at 25.0 ± 2.0 (°C), relative humidity of 60–70 (%), and a 14-hour photoperiod. Plants were cultivated in pots containing a standardized soil mixture and watered regularly to maintain optimal moisture levels.

Measurements were taken up to the V3 phenological stage of plant development. During the experiment (21 days), the plants were divided into two groups:

- **Irrigated (10 days):** Continued to receive regular irrigation to maintain field capacity.
- **Non-irrigated (11 days):** Subjected to water stress by withholding irrigation to reduce soil moisture content gradually.

The techniques and methods involve the direct manipulation of water availability, observation of dehydration symptoms (loss of turgor), quantification of growth response (biomass), and analysis of underlying physiological mechanisms (proteins and soluble sugars). Furthermore, environmental factors affecting water demand (such as humidity, a component of VPD) are considered crucial for accurate modeling of water stress. [26] [27]

B. Electronic Nose Setup

The E-nose system used was an Alpha Fox™ 2000, equipped with an array of six Complementary Metal-Oxide Semiconductor (CMOS) sensors. These sensors operate on the metal-oxide semiconductor principle illustrated in Figure 4, where gas adsorption/desorption processes induce measurable resistance changes through electron transfer mechanisms.

The specific equipment used in this study, shown in Figure 5, features a controlled sample injection system and integrated data acquisition interface, enabling precise VOC measurements under standardized conditions.

The Alpha Fox system employed a six-sensor array with specific sensitivities to different VOC classes, as detailed in Table II.

TABLE I
CORE REFERENCES FOR RADAR CHART AREA AS QUANTITATIVE METRIC

Category	Author	Key Contribution
Mathematical Foundation	Borkowski et al. [20]	Formal proofs for radar chart polygons as synthetic meters
Engineering	Peng et al. [18]	Radar Chart Index (RCI) with area metrics
	Li et al. [17]	Area/perimeter vectors for wind power evaluation
Biomechanics	Porter & Niksiar [21]	Polygon area for biological materials performance
Statistical Methods	Wang et al. [19]	PCA integration with polygon area indicator

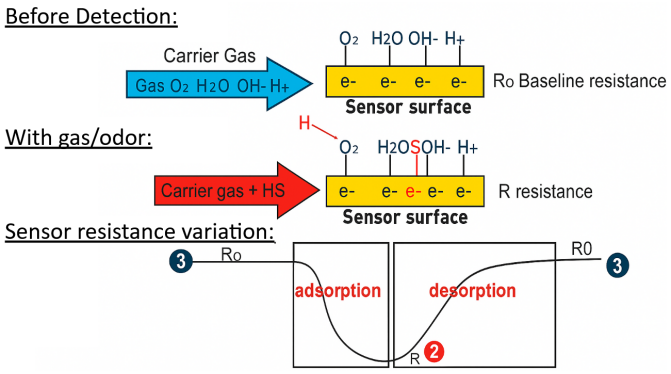

Fig. 4. Operating principle of metal-oxide semiconductor (MOS) sensors showing adsorption/desorption processes and corresponding resistance changes. Red arrows indicate electron transfer during gas detection [29].

Fig. 5. Commercial Alpha Fox™ 2000 electronic nose system used in experiments [29].

TABLE II
THE SENSORS INSTALLED IN THE E-NOSE AREA [28].

No.	Sensor	Sensitivity property	Reference Materials
S1	T30/1	Organic compounds	Organic compounds
S2	P10/1	Combustible gas	Hydrocarbon
S3	P10/2	Inflammable gas	Methane
S4	P40/1	Oxidizing gas	Fluorine
S5	T70/2	Aromatic compounds	Methyl benzene, xylene
S6	PA/2	Organic compounds and toxic gas	Ammonia, amines, ethyl alcohol

C. Chamber Design and Instrumentation

The experimental setup included a specially designed chamber (Figure 6) with dimensions d=25.0 cm, height=57.0 cm, and volume=27.93 L, equipped with complementary sensors for monitoring environmental parameters [2]. The chamber, constructed from Poly(methyl methacrylate) (PMMA) with 92% transmittance in the visible range [30], was instrumented to measure:

- Temperature (T in °C) using digital thermometers with 0.1°C resolution
- Relative humidity (RH in %) with 0.5% resolution sensors
- CO_2 concentration (0–2,000 ppm range) using Vaisala probes
- Natural light intensity (0.001–19.9 K lumen/m^2)

Continuous monitoring was performed at 5-minute intervals, creating a comprehensive environmental database alongside E-nose measurements [2]. The chamber design included a computer fan to simulate wind (28.32 L/min) and an irrigation system that allowed water administration without compromising chamber insulation.

D. Soil Specifications and Isolation

The experiment utilized dystrophic Red Yellow Latosol (LVAd) with specific granulometry: 369 g/kg clay, 54 g/kg silt, and 577 g/kg sand. Soil moisture was maintained at field capacity (0.295 cm^3/cm^3 at 10 kPa) during irrigation phases and reached the permanent wilting point (0.134 cm^3/cm^3 at -1,500 kPa) during stress phases.

To isolate transpiration effects, the soil was covered with aluminum foil, effectively eliminating gas exchange between the rhizosphere and the chamber atmosphere. This isolation method, consistent with approaches validated for soybean transpiration studies [31], ensured that measured VOC emissions originated primarily from plant physiological processes rather than soil microbial activity.

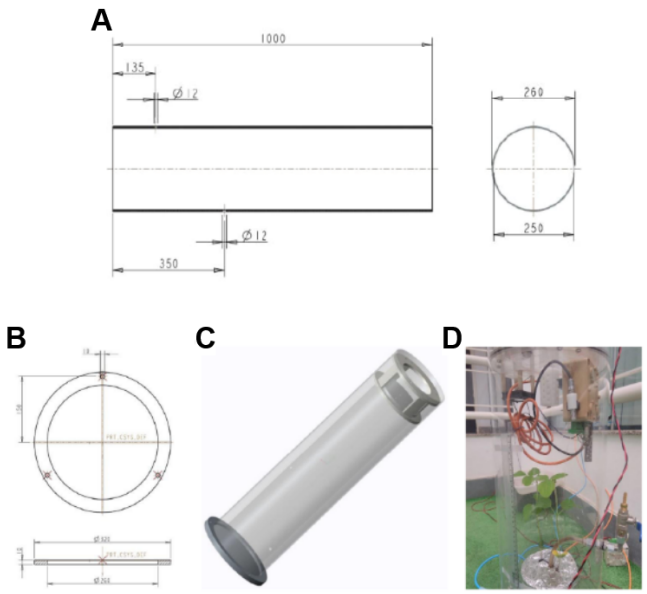

Fig. 6. Experimental chamber design for soybean VOC monitoring. Key specifications: 250 mm internal diameter × 570 mm height (27.93 L volume). Components shown: (A) Dimensional schematic, (B) Base plate with sensor/irrigation interfaces, (C) Assembly diagram, (D) Operational setup with plant specimen.

E. Gas Sampling Using the Headspace Protocol

The headspace sampling technique using a 2,500 µL syringe with PTFE seal provided precision of ¡ ±1% volume accuracy. Baseline measurements from the empty chamber over three days established reference conditions: temperature variation of 4.0°C (23.0–27.0°C), relative humidity variation of 9.0% (16–25%), and CO_2 variation of 20.0 ppmv (250–270 ppmv). These controlled baseline measurements ensured that subsequent plant-emitted VOC detections were not confounded by chamber artifacts.

The sampling volume of 500 µL at a flow rate of 150 mL/min was optimized to balance signal intensity with chamber disturbance minimization, based on preliminary sensitivity tests.

F. Applications in Electronic Nose

The sensitivity S (%) for each sensor was calculated using Equation (3):

$$S(\%) = \left(\frac{R - R_0}{R_0}\right) \times 100\,(\%) \tag{3}$$

where:

- R_0 – Initial electrical resistance (Ω);
- R – Electrical resistance varying over time (Ω).

To analyze the data obtained from the E-nose, we utilized both radar charts and radar area charts to represent the peak sensitivity (S (%)) for each of the six sensors: S1 T30/1, S2 P10/1, S3 P10/2, S4 P40/1, S5 T70/2, and S6 PA/2. This data was normalized using Equation (3) and is shown in Figure 7.

A radar area chart is a specific type of radar chart that illustrates the values by displaying the area enclosed by the lines connecting the data points. Figure 8 presents the representation of both the radar chart and the radar area chart for the peak sensitivity (S (%)) across all sensors. Radar charts are particularly useful for visualizing multiple variables simultaneously [32].

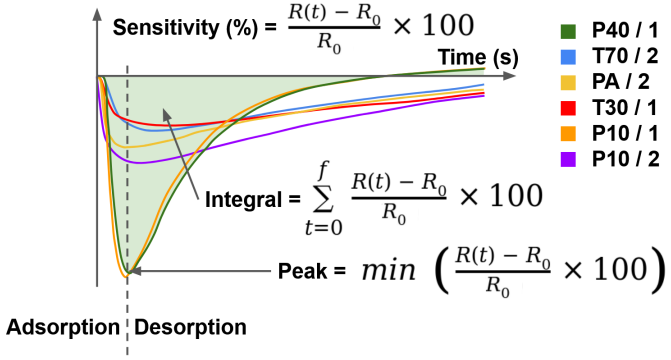

Fig. 7. The variation in sensitivity, using Equation (3), of each of the six sensors in relation to time, depending on the gas sampled and measured in the E-nose.

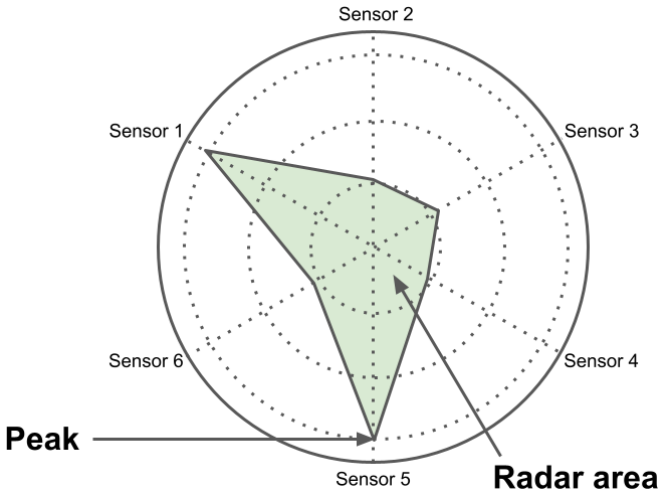

Fig. 8. The radar chart and the radar area chart from the sensitivity (%) peak for the six sensors (S1: T30/1; S2: P10/1; S3: P10/2; S4: P40/1; S5: T70/2; and S6: PA/2) from the E-nose.

G. Data Processing from E-Nose Responses

1) Data Processing from E-Nose Responses: The transformation of raw sensor signals into quantitative metrics followed the workflow depicted in Figure 9. This systematic approach ensured consistent feature extraction across all measurements.

The raw E-nose data, consisting of resistance-time curves for each of the six sensors during 240-second adsorption/desorption cycles, was processed to extract quantitative features. For each sensor response curve $r_i(t)$, where $i = 1, \ldots, 6$ represents the sensor index and t represents time in seconds, two key metrics were computed (Figures 7 and 8):

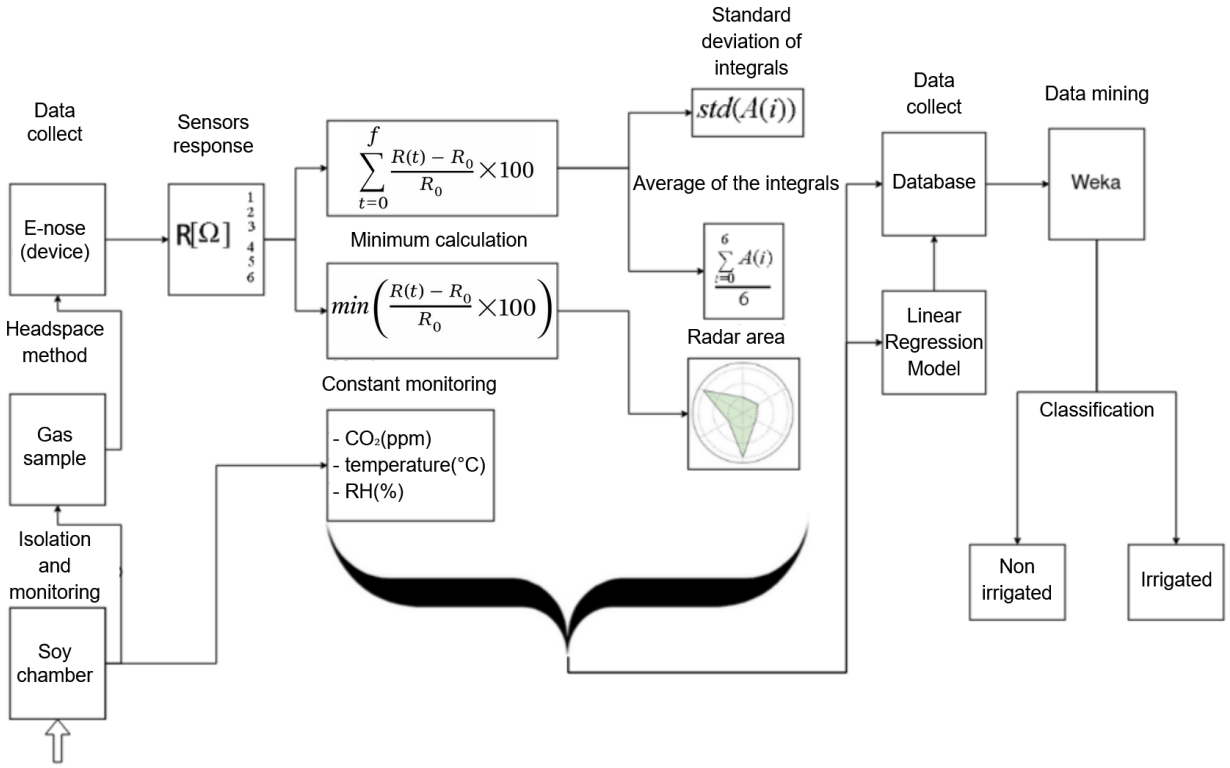

Fig. 9. Data processing workflow from raw sensor responses to derived metrics. Steps include: (1) Raw resistance-time curves for six sensors, (2) Calculated sensitivity profiles, (3) Peak detection and area calculation, (4) Radar chart construction from normalized peaks.

- **Area under the curve:** $A_i = \sum_{t=0}^{240} |\frac{r_i(t)-r_i(0)}{r_i(0)}|$, representing the cumulative response intensity over the measurement period
- **Peak sensitivity:** $P_i = \min_{t\in[0,240]} \frac{r_i(t)-r_i(0)}{r_i(0)} \times 100\%$, representing the maximum response amplitude

These metrics were computed for all three replicates (3 × 500 µL samples) taken during each measurement session (morning and afternoon). The radar chart area A_n was subsequently calculated from the normalized peak sensitivity values P_i of all six sensors, providing a composite measure of overall sensor array response.

The processing pipeline ensured robust feature extraction by:

1) Computing baseline resistance $r_i(0)$ from stable pre-injection measurements
2) Normalizing responses across sensors to account for differential sensitivities
3) Averaging triplicate measurements to reduce sampling variability
4) Validating data quality through response curve shape analysis

H. Experimental Protocol Refinements

The methodology evolved through three experimental phases, as summarized in Table III. These iterative refinements enhanced measurement reliability while addressing technical challenges identified in earlier trials.

The study incorporated iterative protocol improvements across multiple experimental iterations with six soybean specimens:

- **Sample volume optimization:** Increased from single 500 µL samples to 1,500 µL samples (3 × 500 µL replicates) for improved statistical robustness and outlier detection
- **Temporal coverage:** Expanded from single daily measurements to both morning (9:30 AM) and afternoon (3:30 PM) sessions to capture diurnal variability
- **Environmental controls:** Implemented dry air purging systems in later experiments to maintain consistent chamber humidity levels
- **Extended monitoring:** Prolonged irrigation periods for selected specimens to decouple plant developmental age from water stress effects

These refinements, developed through systematic experimentation, enhanced data quality and enabled more robust pattern recognition in subsequent analyses while maintaining the non-invasive nature of the measurements.

I. Calculating the Area of a Radar Chart

A radar chart is a graphical representation that effectively illustrates multidimensional data by expressing the values of each attribute in a clear and concise manner. Its 2D visualization provides a comprehensive view of the data, making it easier to analyze and understand its various dimensions [33].

The method of radar chart for Multidimensional Data: $X = \{X_1, X_2, \ldots, X_j, \cdots X_n\}$ is a multi-dimensional data set, and $X_i = \{x_{i1}, x_{i2}, x_{i3}, \ldots, x_{iN}\}$ is a N-dimensional vector. Use the radar chart when $N \geqslant 3$ [33].

A method for evaluating the accessibility of a facility location using the area of a radar chart was provided by Takenaka et al. [16]. The authors argue that the area of a radar chart is a more stable measure of accessibility than other measures.

The radar values were calculated using the absolute value of the minimum values in Equation (3) for each sensor, where:

$$X_i = S_i = \{S_1(\%), S_2(\%), S_3(\%), S_4(\%), S_5(\%), S_6(\%)\} \tag{4}$$

To calculate the area (A_n) of the polygon formed in a radar chart:

1) **Convert Polar Coordinates to Cartesian Coordinates.** Each data point is defined by:
   - r_i: The distance from the center to the data point along axis i (the normalized value of the variable).
   - θ_i: The angle corresponding to axis i .

   The Cartesian coordinates (x_i, y_i) are related to the polar coordinates (r_i, θ_i) by the formulas:

$$x_i = r_i \cos\theta_i, \quad y_i = r_i \sin\theta_i \tag{5}$$

2) **Apply the Shoelace Formula:** The area of the polygon can be calculated using the Shoelace Formula (6):

$$A_n = \frac{1}{2}\left|\sum_{i=1}^{n}(x_i y_{i+1} - x_{i+1} y_i)\right| \quad (\%^2) \tag{6}$$

where $x_{n+1} = x_1$ and $y_{n+1} = y_1$ to complete the loop.

The formula sums the cross-products of vertex coordinates in a specific order [2].

J. S-Norm: Geometric Interpretation of the Radar Area

The area of the polygon is crucial because the square of the vector's S-norm is equal (minus a multiplicative constant) to the area of the polygon formed by the radar graph of these vectors.

a) Definition of the S-Scalar Product and the S-Norm: The formalism relies on the concept of the S-operator (S), which is an *S-shift* (displacement) operator defined for a vector $x = (x_1, x_2, \ldots, x_n) \in X = \mathbb{R}^n$ as $Sx := (x_2, x_3, \ldots, x_n, x_1)$.

The S-scalar product is defined by the formula:

$$\langle x, y\rangle_S := \langle x, Sy\rangle \tag{7}$$

where $\langle\cdot\rangle$ represents the standard scalar product.

The S-norm of a vector x (denoted $\|x\|_S$) is defined by Formula (8) as:

$$\|x\|_S := |\langle x, x\rangle_S|^{1/2} = \left(\frac{1}{n}\left|\sum_{k=1}^{n} x_k x_{k+1}\right|\right)^{1/2} \tag{8}$$

where $x = (x_1, x_2, \ldots, x_n)$, and x_{n+1} is defined as x_1.

b) Geometric Interpretation and Area Formula: Assuming that the vector $x = (x_1, x_2, \ldots, x_n) \in \mathbb{R}^n$ has coordinates $1 \geq x_i \geq 0$, the graphical representation utilizes an n-regular polygon inscribed in a unit circle (radius $r = 1$) with the center at the origin. The coordinates x_i are represented as points x_i on the 0_i axes emanating from the center.

By connecting the points in order (x_1 to x_2, x_2 to x_3, …, x_n to x_1), an n-polygon is obtained.

The area (S_1) of this polygon (induced by vector x) is defined by the formula:

$$S_1 = \sum_{i=1}^{n} \frac{1}{2} x_i x_{i+1} \sin\left(\frac{2\pi}{n}\right) \tag{9}$$

This formula can be rewritten in terms of the squared S-norm:

$$S_1 = \frac{1}{2}\sin\left(\frac{2\pi}{n}\right)\sum_{i=1}^{n} x_i x_{i+1} = \frac{1}{2} n \sin\left(\frac{2\pi}{n}\right)\|x\|_S^2 \tag{10}$$

where $x_{n+1} := x_1$.

IV. Results and Discussion

The average values and standard deviations derived from radar measurements of both irrigated and non-irrigated soybean samples are illustrated in Figure 10.

A. Temporal Variability and Diurnal Patterns

TABLE III
Experimental iterations and protocol refinements across six soybean specimens

Specimen	Sampling Protocol	Environmental Controls	Key Refinements
Plants 1-3	Single 500 µL samples	Basic chamber monitoring	Baseline methodology establishment
Plant 4	3 × 500 µL replicates	Dry air purging implemented	Improved statistical robustness
Plants 5-6	Morning/afternoon sessions	Open chamber periods	Diurnal pattern capture

The experimental design captured distinct diurnal patterns in VOC emissions, with measurements taken at 9:30 AM (morning) and 3:30 PM (afternoon) [2]. Morning measurements consistently showed lower standard deviations in radar area calculations and more stable sensor response patterns. In contrast, afternoon measurements exhibited increased variability, particularly in response to environmental fluctuations such as light intensity changes.

This temporal variability is evident in Figure 10, where afternoon sessions show greater standard deviations. The most pronounced variation occurred on the 22nd day, characterized by overcast conditions with intermittent rain, resulting in luminosity variations of approximately 77% during afternoon measurements compared to 39% in the morning [2].

TABLE IV
MACHINE LEARNING CLASSIFICATION PERFORMANCE FOR WATER STRESS DETECTION.

Algorithm	Major Accuracy Obtained (%)
Decision Tree	93.6
k-NN (k=3)	80.7
Logistic Regression	78.2

B. Environmental Parameter Correlations

Complementary environmental measurements revealed significant patterns [2]:

- Chamber temperature consistently exceeded laboratory environment by 2–4°C, with maximal differences observed in afternoon measurements.
- CO_2 concentrations inside the chamber were typically 50–100 ppm lower than external levels during active photosynthesis periods.
- Relative humidity within the chamber exceeded external levels by 15–25% during morning measurements.

These environmental interactions, consistent with plant physiological responses to water stress [34], [35], contextualize the E-nose responses and highlight the importance of standardized measurement conditions for agricultural applications.

C. Synthesis with Machine Learning Validation

The radar area methodology developed in this study aligns with and complements machine learning approaches applied to the same experimental system. Comparative performance analysis of three machine learning algorithms (Table IV) achieved 93.6% classification accuracy using Decision Tree algorithms on comprehensive datasets incorporating both E-nose responses and environmental parameters [36].

1) Machine Learning Pipeline Implementation: A comprehensive machine learning pipeline was implemented using the WEKA toolkit (Figure 11), incorporating:

1) **Data balancing:** Equalizing irrigated and non-irrigated samples to prevent classifier bias
2) **Feature normalization:** Scaling all numerical features to [0,1] range for algorithm compatibility
3) **Algorithm evaluation:** Comparative testing of Decision Trees, k-Nearest Neighbors (KNN), and Logistic Regression
4) **Validation strategies:** Three-fold validation using training set evaluation, cross-validation, and independent test set validation

D. Analysis of Measurement Variability

The data reveal a marked difference between the measurements taken in the morning and those taken in the afternoon, with the greatest standard deviation observed during the afternoon sessions.

This pronounced variation may be attributed to several influencing factors, including the physiological state of the plants, which can change due to water uptake and nutrient availability.

Environmental conditions at the time of sample extraction also likely played a significant role; the fluctuating temperatures, humidity levels, and light intensity throughout the day can affect the plants' responses. Furthermore, the specific growth stage of the soybeans—whether they are in vegetative growth or nearing maturation—can impact how they interact with their environment. Additionally, potential errors in the syringe headspace during sampling could introduce variability in the measurements.

It is particularly noteworthy that the highest standard deviation was recorded during the afternoon. On the 22nd day of the experiment, specific weather conditions were present, characterized by overcast skies, intermittent rain, and significant cloud cover. These factors likely influenced the plants' physiological responses, contributing to the observed variability in the data.

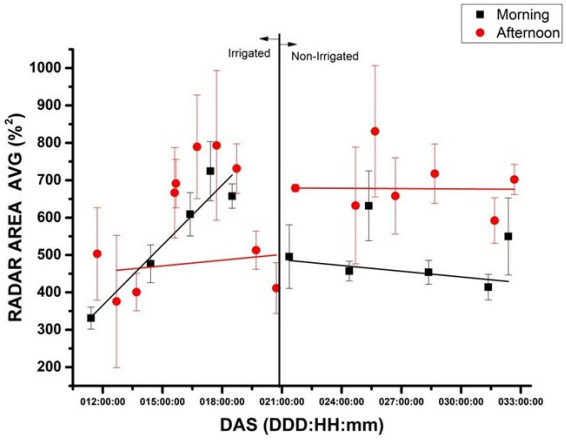

Fig. 10. E-nose measurements of gas samples taken from a chamber containing soybeans during the Days After Sowing (DAS), using the average radar area and standard deviation ($n = 3$). The measurements are presented based on the time of day, either in the morning (9:30 a.m.) denoted by red circles or in the afternoon (3:30 p.m.) denoted by black squares. Moreover, the measurements are obtained from both irrigated and non-irrigated plants. For each DAS, gas samples are measured three times in both periods, i.e., the morning and afternoon, to obtain the radar area measurement.

E. Sensor Performance Analysis

Individual sensor analysis revealed differential sensitivity patterns: sensors P10/1 (combustible gas/hydrocarbon) and P40/1 (oxidizing gas/fluorine) showed the highest responsiveness to water stress-induced VOC changes. During irrigated conditions (DAS 11–21), peak sensitivity for P10/1 was -27.97% ± 4.36%, while during water stress (DAS 22–32) it was -28.62% ± 3.26%. For P40/1, corresponding values were -28.30% ± 4.87% and -28.88% ± 3.59%.

The negative sensitivity values indicate decreased electrical resistance upon gas exposure, reflecting increased sensor conductivity in response to specific VOC compounds emitted by water-stressed plants.

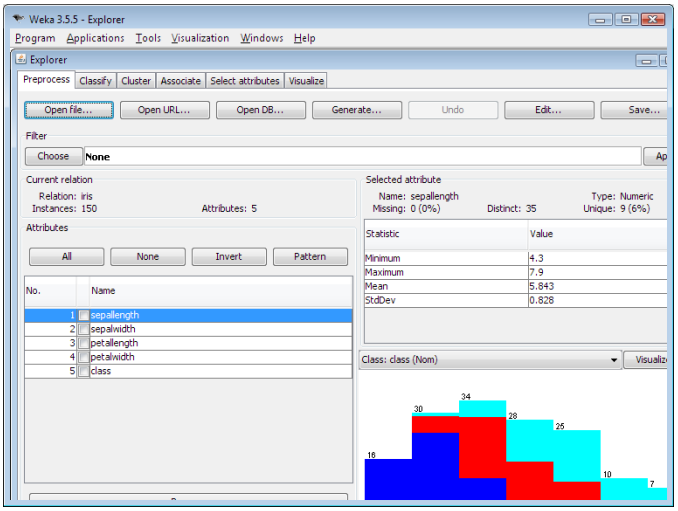

Fig. 11. WEKA (Waikato Environment for Knowledge Analysis) software interface showing the machine learning workflow [37].

F. Methodological Validation and Limitations

The experimental approach addressed several methodological challenges:

- Chamber design minimized environmental interference while maintaining plant viability
- Soil isolation controlled for non-plant VOC sources
- Temporal standardization reduced diurnal variability effects
- Multiple measurement replicates (n=3 per time point) ensured statistical robustness

Notably, the 22nd day of experimentation presented unique conditions with overcast skies and intermittent rain, resulting in the highest observed standard deviations. These conditions provided valuable insight into environmental sensitivity and highlight the importance of meteorological considerations in field applications.

V. Conclusion and Future Work

The radar area chart is a specialized variant of the radar chart that utilizes the area enclosed by the connecting lines of data points to visually represent and compare values. Figure 8 illustrates this radar chart format, specifically highlighting the radar area at the sensitivity peak (S (%)), which indicates the maximum responsiveness of the variables in question.

Radar area charts are particularly valuable tools when analyzing and comparing the overall performance of distinct data groups, for example, across different experimental conditions. This visual representation facilitates the interpretation of complex multivariate sensor data, enabling researchers to quickly identify patterns and trends relevant to plant stress detection. The area can be used as a valid metric to rank data.

The key findings demonstrate that:

- The radar chart area metric effectively distinguished irrigated from non-irrigated soybean plants, showing a clear divergence after the onset of water stress.
- Sensor-specific analysis identified S2 (P10/1) and S4 (P40/1) as the most responsive to water-stress-induced VOC changes.
- Measurements exhibited significant diurnal variability, with morning sessions (9:30 AM) providing more stable and consistent radar area values compared to afternoon sessions (3:30 PM), underscoring the importance of standardized sampling times.
- The geometric interpretation of the area, supported by the mathematical formalism of the S-norm, provides a solid theoretical foundation for using polygon area as a synthetic indicator of overall sensor array response.

The integration of this area-based metric with machine learning validation (achieving up to 93.6% classification accuracy) confirms its utility as a discriminative feature for automated stress detection systems. By capturing early, non-visible VOC pattern shifts, this methodology enables a proactive approach to irrigation management, potentially preventing yield losses before visual symptoms appear.

Future work directions include integrating the method with equipment in a mobile unit to facilitate field use and applying the methodology to study thermal and water stress.

Initial studies with wheat, aimed at investigating water stress, are being carried out using the proposed technique and methodology, and are not limited to soybeans.

Acknowledgment

This work was supported by Embrapa Instrumentation and Embrapa project # 20.22.01.001.00. The authors extend their gratitude to Dr. Ednaldo José Ferreira from Embrapa Instrumentation, the Embrapa-Bayer project 10.20.05.006.00.00, and the teams at LANAPRE and LNNA for providing experimental facilities and materials. Additional acknowledgments are due to CAPES-CNPq for doctoral fellowships and to ICMC-USP for institutional support.

References

[1] P. S. d. P. Herrmann and M. S. Lucas, "Using radar chart areas to evaluate the sensitivity of electronic nose sensors in detecting water stress in soybean," *ALLSENSORS*, 2025, thinkMind Digital Library, https://www.thinkmind.org.

[2] P. S. D. P. Herrmann, M. d. Santos Luccas, E. J. Ferreira, and A. Torre Neto, "Application of electronic nose and machine learning used to detect soybean gases under water stress and variability throughout the daytime," *Frontiers in Plant Science*, vol. 15, p. 1323296, 2024.

[3] D. Materić, D. Bruhn, C. Turner, G. Morgan, N. Mason, and V. Gauci, "Methods in plant foliar volatile organic compounds research," *Applications in Plant Sciences*, vol. 3, no. 12, p. 1500044, 2015.

[4] S. Zorpeykar, E. Mirzaee-Ghaleh, H. Karami, Z. Ramedani, and A. D. Wilson, "Electronic nose analysis and statistical methods for investigating volatile organic compounds and yield of mint essential oils obtained by hydrodistillation," *Chemosensors*, vol. 10, no. 11, p. 486, 2022.

[5] K. W. Kolence and P. J. Kiviat, "Software unit profiles & kiviat figures," *ACM SIGMETRICS Performance Evaluation Review*, vol. 2, no. 3, pp. 2–12, 1973.

[6] M. J. Saary, "Radar plots: a useful way for presenting multivariate health care data," *Journal of Clinical Epidemiology*, vol. 61, no. 4, pp. 311–317, 2008.

[7] Embrapa Soja, "Soja em números," https://www.embrapa.br/en/soja/cultivos/soja1/dados-economicos, 2025, accessed in: 15 Dec. 2025.

[8] O. Basal and A. Szabó, "Physiology, yield and quality of soybean as affected by drought stress," Tech. Rep., 2020.

[9] F. Fiorani and U. Schurr, "Future scenarios for plant phenotyping," *Annual Review of Plant Biology*, vol. 64, no. 1, pp. 267–291, 2013.
[10] B. Niederbacher, J. Winkler, and J. Schnitzler, "Volatile organic compounds as non-invasive markers for plant phenotyping," *Journal of Experimental Botany*, vol. 66, no. 18, pp. 5403–5416, 2015.
[11] R. Jansen, J. Wildt, I. Kappers, H. Bouwmeester, J. Hofstee, and E. Van Henten, "Detection of diseased plants by analysis of volatile organic compound emission," *Annual Review of Phytopathology*, vol. 49, no. 1, pp. 157–174, 2011.
[12] M. G. Hale and D. M. Orcutt, *The Physiology of Plants under Stress*. New York, USA: Wiley, 1987.
[13] M. G. Mostofa, A. Sahu, Y. Xu, I. Basrai, L. Doron, V. Lefrancois, and T. D. Sharkey, "Cryptic isoprene emission of soybeans," *Proceedings of the National Academy of Sciences*, vol. 122, no. 24, p. e2502360122, 2025.
[14] V. Ludwig, M. R. P. Berghetti, S. R. Ribeiro, F. P. Rossato, L. M. Wendt, F. R. Thewes, F. R. Thewes, A. Brackmann, V. Both, and R. Wagner, "The effects of soybean storage under controlled atmosphere at different temperatures on lipid oxidation and volatile compounds profile," *Food Research International*, vol. 147, p. 110483, 2021.
[15] T. R. Sinclair, C. D. Messina, A. Beatty, and M. Samples, "Assessment across the united states of the benefits of altered soybean drought traits," *Agronomy Journal*, vol. 102, no. 2, pp. 475–482, 2010.
[16] T. Takenaka, K. Nakamura, T. Ukai, and Y. Ohsawa, "Stability of the area of radar chart to evaluate the accessibility of facility location," *J. City Plann. Institute Japan*, vol. 53, no. 3, pp. 640–645, 2018.
[17] G. Li, G. Li, and M. Zhou, "Comprehensive evaluation model of wind power accommodation ability based on macroscopic and microscopic indicators," *Protection and Control of Modern Power Systems*, vol. 4, no. 3, pp. 1–12, 2019.
[18] W. Peng, Y. Li, Y. Fang, Y. Wu, and Q. Li, "Radar chart for estimation performance evaluation," *IEEE Access*, vol. 7, pp. 113 880–113 888, 2019.
[19] D. Wang, Y. Wan, X. Wang *et al.*, "Improved radar chart based on principal component and its application in comprehensive evaluating," *J. Appl. Stat. Manag*, vol. 29, no. 5, pp. 883–889, 2010.
[20] B. Borkowski, A. Wiliński, W. Szczesny, and Z. Binderman, "Mathematical analysis of synthetic measures based on radar charts," *Mathematical Modelling and Analysis*, vol. 25, no. 3, pp. 473–489, 2020.
[21] M. M. Porter and P. Niksiar, "Multidimensional mechanics: Performance mapping of natural biological systems using permutated radar charts," *PloS one*, vol. 13, no. 9, p. e0204309, 2018.
[22] A. Reske Filho, "Aplicação do gráfico radar na avaliação do desempenho das empresas de construção civil," Ph.D. dissertation, 2014.
[23] A. A. Zakharova, D. A. Korostelyov, and O. N. Fedonin, "Mathematical support and software of visual filtering of alternatives in multi-criteria decision making problems," in *CEUR Workshop Proceedings*. CEUR-WS.org, 2019, pp. 82–85.
[24] F. Ye, Y. Chen, and Q. Huang, "A study of the visualization tool for computer science majors' capability assessment," *International Journal of Information and Education Technology*, vol. 9, no. 1, pp. 61–65, 2019.
[25] C. P. Pereira, D. P. Paes, D. M. Prata, and L. P. Monteiro, "Desenvolvimento de índice de comparação de ecoeficiência a partir de ecoindicadores," *Sistemas & Gestão*, vol. 9, no. 2, pp. 168–180, 2014.
[26] R. S. Kong and H. A. Henry, "Interactions of plant growth responses to spring freezing and summer drought: a multispecies comparison," *American Journal of Botany*, vol. 106, no. 4, pp. 531–539, 2019.
[27] E. Kirchhof, F. Campos-Arguedas, N. S. Arias, and A. P. Kovaleski, "Thresholds for spring freeze: measuring risk to improve predictions in a warming world," *New Phytologist*, vol. 248, no. 2, pp. 563–575, 2025.
[28] W. Wei, J. Li, and L. Huang, "Discrimination of producing areas of astragalus membranaceus using electronic nose and uhplc-pda combined with chemometrics." *Czech Journal of Food Sciences*, vol. 35, no. 1, 2017.
[29] FOX Analyzer, *Hardware User's Guide – Manuel Number 001*, 2000, alpha Fox^{TM} 2000 Electronic Nose System.
[30] P. E. Keller and R. T. Kouzes, "Water vapor permeation in plastics," no. PNNL-26070, 2017. [Online]. Available: https://www.osti.gov/servlets/purl/1411940
[31] L. C. Ferreira, W. Neiverth, L. F. F. Maronezzi, R. N. R. Sibaldelli, A. L. Nepomuceno, J. R. B. Farias, and N. Neumaier, "Efficiency of cover materials in preventing evaporation in drought-stressed soybeans grown in pots." *Revista de Ciências Agrárias*, vol. 58, no. 4, pp. 359–365, 2015.
[32] W.-Y. Liu, B.-W. Wang, J.-X. Yu, F. Li, S.-X. Wang, and W.-X. Hong, "Visualization classification method of multi-dimensional data based on radar chart mapping," in *2008 International Conference on Machine Learning and Cybernetics*, vol. 2. IEEE, 2008, pp. 857–862.
[33] W. Peng, "Improved radar chart for lighting system scheme selection," *Applied Optics*, vol. 61, no. 19, pp. 5619–5625, 2022.
[34] H. Lambers and R. S. Oliveira, "Plant water relations," in *Plant Physiological Ecology*. Springer, 2019, pp. 187–263.
[35] J. Pallas Jr, "Transpiration and stomatal opening with changes in carbon dioxide content of the air," *Science*, vol. 147, no. 3654, pp. 171–173, 1965.
[36] P. S. P. Herrmann and M. Santos Luccas, "Utilização do "e-nose" e "machine learning" para investigação da emissão de gases da soja submetida a estresse hídrico," Embrapa Instrumentação, Relatório Técnico PIBIC/CNPq Processo CNPq 129877/2019-0, 2020.
[37] Wikipedia contributors, "Weka (software)," https://pt.wikipedia.org/wiki/Weka, 2025, accessed in: 15 Dec. 2025.